Energy transfer due to shoaling and decomposition of breaking and non-breaking waves over a submerged bar

Arun Kamath*, Mayilvahanan Alagan Chella, Hans Bihs, Øivind A. Arntsen

Department of Civil and Environmental Engineering, Norwegian University of Science and Technology (NTNU), 7491 Trondheim, Norway

Engineering Applications of Computational Fluid Mechanics, 2017, **11** (1), pp. 450-466.
DOI: http://dx.doi.org/10.1080/19942060.2017.1310671

Abstract

Wave propagation over a submerged bar is simulated using the open source CFD model REEF3D with various incident wave heights to study shoaling, wave breaking features and the process of wave decomposition into higher harmonics for relatively long waves of $kd = 0.52$. The computed free surface elevations are compared with experimental data and a good agreement is obtained for both non-breaking and spilling breaking waves for both the wave phase and free surface elevation which has been difficult to obtain in current literature. The differences in the mode of wave shoaling over the weather side slope and the wave decomposition over the lee side slope of the submerged bar are discussed. The evolution of spilling breakers and plunging breakers over the bar crest is also studied. It is found that the free surface elevation continuously increases due to shoaling in the case of non-breaking waves, whereas breaking waves propagate with much lower free surface elevations after breaking over the bar crest. The power spectra of the free surface elevations at various locations indicate that the wave energy in the fundamental frequency is reduced by 76% for the non-breaking wave with $kA = 0.015$ and by about 90% in other cases with higher incident wave heights with $kA = 0.023 - 0.034$ due to energy dissipation and energy transfer to higher harmonic components as the wave propagates over the submerged bar.

Keywords: wave decomposition; wave breaking; shoaling; submerged bar; numerical wave tank; CFD; REEF3D

*Corresponding author, hans.bihs@ntnu.no

Postprint, published in Engineering Applications of Computational Fluid Mechanics, doi:http://dx.doi.org/10.1080/19942060.2017.1310671

1 Introduction

Wave propagation in shallow waters is influenced by the sea bottom topography and wave transformation processes such as diffraction, shoaling and wave breaking. Wave shoaling refers to the phenomenon where the incident wave height is changed as the deep water wave propagates to water depths less than half the wavelength. Shoaling results in asymmetry in the wave profile with sharper crests and shallower troughs, creating an imbalance in the local wave energy distribution and leading to wave deformation (Adeyemo, 1968). The wave crest heights reach a limiting value, beyond which the wave breaks to balance the local increase in the wave energy. The additional challenge in wave propagation over a submerged obstacle is the wave decomposition process which occurs behind the obstacle, in the region of increasing water depth, leading to the evolution of higher-order harmonics and rapidly varying waveforms. These processes can only be represented in a numerical model, which accounts for nonlinearity and has good dispersion characteristics (Beji and Battjes, 1994).

The accurate evaluation of the wave kinematics in the near-shore area is important due to their impact on hydrodynamic properties such as wave forces, wave run-up and sediment transport. The mode of wave breaking is generally classified using the surf similarity parameter, $\xi = \frac{tan\alpha}{\sqrt{H/L_0}}$, where α is the angle of the slope, H is the incident wave height over the toe of the slope and $L_0 = \frac{g}{2\pi}T^2$ is the deep water wavelength where T is the wave period. Battjes (1974) presented the relationships between ξ and various flow parameters, and also the classification of breaker types on emergent plane sloping beaches. Gourlay (1994) carried out experiments on waves breaking on a submerged reef and Blenkinsopp and Chaplin (2008) on a submerged slope and found out that the classification presented by Battjes (1974) for emergent sloping beaches is not directly applicable for submerged structures. Wave propagation over submerged structures has been studied through experimental investigations on a submerged bar (Beji and Battjes, 1993), a rectangular obstacle (Chang et al., 2001) and processes such as wave decomposition and vortex generation have been identified. Numerical modeling of wave propagation over a submerged obstacle has been carried out using Boussinesq equations (Beji and Battjes, 1994; Bosboom et al., 1996; Brocchini et al., 1992) and shallow water equations (Kobayashi et al., 1987) with good results for the wave shoaling process. Lemos (1992) was the first to present simulations of breaking waves using the Reynolds Averaged Navier-Stokes (RANS) equations. Lin and Liu (1998) and Zhao et al. (2004) employed single-phase CFD (Computational Fluid Dynamics) models to simulate breaking waves, which could not account for the air-water interaction responsible for the complex free surface deformations (Christensen, 1998).

The knowledge of wave transformation and transmission across submerged structures finds its application in coastal protection measures such as submerged breakwaters, ecological conservation and recreational measures such as artificial reefs. The wave decomposition process modifies the waves transmitted over the submerged structure and this can be usefully exploited in a combined submerged bar- floating breakwater coastal protection measure. For the design of recreational artificial reefs and bars, it is essential to have a better idea regarding the breaking wave characteristics on the crest of the bar to provide sufficient breaker heights for surfing. It has been presented in previous studies on wave breaking that the wave breaking characteristics vary significantly under different breaking conditions (Battjes, 1974; Gourlay, 1994; Blenkinsopp and Chaplin, 2008). In addition, the many existing numerical and theoret-

ical models for wave transformation over submerged breakwaters are based on the potential flow assumption, which cannot describe the rotational flow that occurs during the breaking process (Brocchini, 2013). Numerical modeling of shallow water flows (Lai and Khan, 2012; Muttil and Chau, 2007), in estuaries (Chau and Jiang, 2004, 2001; Wu and Chau, 2006) and over hydraulic structures (Haun et al., 2011) have been numerically investigated by several authors. CFD modeling solves the fluid flow problem by solving the Navier-Stokes equations, accounting for most of the fluid physics with few assumptions. This method has been previously applied to the simulation of breaking waves over a slope by Hieu et al. (2004) and Jacobsen et al. (2012) using a Volume of Fluid (VoF) -based interface capturing method and Alagan Chella et al. (2015) using the level set method to obtain the interface. Alagan Chella et al. (2015) obtained good agreement to experimental data, with a sharp representation of the breaking wave and the formation air pockets, due to the higher order discretization schemes used in the model along with the level set method, compared to the lower order schemes used in previous studies. Numerical modeling with a two-phase CFD model can account for the wave breaking process with few assumptions. Along with higher order discretization schemes and sharp interface capturing, it can account for the complex free surface process involved during wave transformation including breaking and decomposition.

Several studies have been carried out using Large Eddy Simulations (LES) representation of the turbulence in the Navier-Stokes equations such as Christensen and Deigaard (2001), Hieu et al. (2004), Zhao et al. (2004), Watanabe et al. (2005), Christensen (2006), Lubin et al. (2006), Mo et al. (2013) to study the wave breaking process. These studies however are restricted to studies on vortex structures under breaking waves, related aspects on turbulence and wave breaking on slopes, but do not present the wave transformation and decomposition process involved in wave propagation over a submerged bar. While LES and Direct Numerical Simulation (DNS) approach to CFD modeling of breaking waves can provide a thorough understanding of the micro-scale turbulent features, they are rather expensive and superfluous for engineering applications. The energy transfer and wave decomposition aspects are important from an engineering point of view to determine the efficiency of submerged structures to dissipate wave energy, which can be well resolved using Reynolds-Averaged Navier-Stokes (RANS) models. With a better understanding of this phenomenon, submerged structures can be used as effective coastal protection measures without causing a large visual impact on the coastline unlike that from an emerged rubble mound breakwater.

In the current study, the open source CFD model REEF3D (Bihs et al., 2016) is used to simulate wave propagation over a submerged bar. The numerical results are compared with the experimental data from Beji and Battjes (1993). Several previous studies regarding this have numerically calculated the wave propagation only for the non-breaking wave cases (Morgan et al., 2010; Roeber et al., 2010; Stelling and Zijlema, 2003). The breaking wave case was modeled by Tissier et al. (2012), but they reported deviations from the experimental observations from the point of wave breaking. Thus, numerical models accounting for both breaking and non-breaking waves over a submerged bar (Beji and Battjes, 1993) with good agreement to experimental data for both the free surface elevation and the wave phase have not been presented in current literature. This is especially true for the longer wave with $T = 2.5$ s, where the wave decomposition process is seen to be much stronger in the experiments compared to the shorter waves with $T = 1$ s (Beji and Battjes, 1994). An initial study for only non-breaking wave shoaling on a submerged bar was presented with comparison to experimental data (Kamath et al., 2015).

In this paper, the study is significantly extended to cover the evolution of spilling and plunging breakers on the bar crest, with comparison of the free surface elevation in the spilling case. In addition, the shoaling process for the different incident waves is examined through the comparison of the relative wave crest elevations, evaluation of the maximum wave crest steepness and the relative phase differences between the primary wave crests of the transformed waves in the different cases. The decomposition process with transfer of wave energy to higher harmonics is also examined using the power spectral density computed from the free surface elevations and the redistribution of the wave energy amongst the harmonics is discussed. The effect of wave breaking on the wave propagation and decomposition process is also discussed. The study also addresses the effect of the lee side slope of the submerged bar on the wave decomposition process. This is essential as the current literature has dealt with in detail on the effect of the weather side slope on the wave shoaling and breaking process but not the details on the wave decomposition on the lee side. This is important for the construction of innovative coastal and harbour protection structures such as a combination of a submerged bar with a floating breakwater. The floating breakwater is efficient at absorbing wavelengths in the order of its width but does not for longer waves. The addition of the submerged bar in front of the floating breakwater can be used to dissipate some wave energy and also decompose the waves into shorter waves that can be effectively absorbed by the floating breakwater.

2 Numerical Model

2.1 Governing equations

The numerical model uses the Reynolds Averaged Navier Stokes (RANS) equations along with the continuity equation to evaluate the fluid flow:

$$\frac{\partial u_i}{\partial x_i} = 0 \tag{1}$$

$$\frac{\partial u_i}{\partial t} + u_j \frac{\partial u_i}{\partial x_j} = -\frac{1}{\rho}\frac{\partial p}{\partial x_i} + \frac{\partial}{\partial x_j}\left[(\nu + \nu_t)\left(\frac{\partial u_i}{\partial x_j} + \frac{\partial u_j}{\partial x_i}\right)\right] + g_i + S \tag{2}$$

where u_i is the ensemble averaged velocity, ρ is the density of the fluid, p is the modified pressure, ν is the kinematic viscosity, $\nu_t = k/\omega$ is the eddy viscosity, k is the turbulent kinetic energy, ω is the specific turbulent dissipation rate, t is time and g is the acceleration due to gravity. The equations are presented in the compact tensor notation and indices i and j are free indices. Surface tension is included in the source term S in Eq. 2, where:

$$S = \sigma\kappa(\phi)\delta(\phi)\frac{\delta\phi}{\delta x_i} \tag{3}$$

where σ is the surface tension coefficient, κ is the curvature of the interface and the surface tension is activated only around the interface using the Dirac delta function $\delta(\phi)$(Peng et al., 1999) and ϕ is the level set function used to obtain the free surface in the model.

The projection method (Chorin, 1968) is used for pressure treatment and the resulting Poisson pressure equation is solved using a preconditioned BiCGStab solver (van der Vorst, 1992). Turbulence modeling is carried out using the two-equation $k-\omega$ model proposed by

Wilcox (1994). Wave propagation is characterized by large gradients in the velocities resulting in a highly strained flow. Since, the production of turbulence in the $k-\omega$ model depends on the gradients in the velocity field, this results in unphysical overproduction of turbulence in a numerical wave tank. A stress limiter in the definition of eddy viscosity using assumption by Bradshaw et al. (1967) as shown by Durbin (2009) is implemented to avoid this. The free surface is a natural boundary for the turbulent eddies which is not accounted for in the k-ω model, resulting in an overproduction of turbulence at the free surface in a two-phase CFD model, due to the large strain caused by the large difference in the density of air and water. Free surface turbulence damping using a limiter around the interface as shown by Naot and Rodi (1982) is carried out to avoid the overproduction of turbulence at the interface. The limiter is activated only around the interface using the Dirac delta function.

2.2 Discretization schemes

The fifth-order conservative finite difference Weighted Essentially Non Oscillatory (WENO) scheme (Jiang and Shu, 1996) is used for the discretization of the convective terms in the RANS equations and the level set function, the turbulent kinetic energy and the specific turbulence dissipation rate are discretized using the Hamilton-Jacobi formulation of the WENO scheme (Jiang and Peng, 2000). Time advancement is carried out using a four-step scheme proposed by Choi and Moin (1994) with implicit treatment of convective and viscous terms. An adaptive time stepping approach is used to satisfy the Courant-Frederich-Lewy (CFL) condition for numerical stability. The numerical model uses a uniform Cartesian grid for spatial discretization facilitating an easy implementation of higher order schemes. The staggered grid approach is used with pressure at the cell centers and velocities at the cell faces, providing a tight coupling between the pressure and the velocity. A local directional ghost cell immersed boundary method (Berthelsen and Faltinsen, 2008) extended to three dimensions is employed to handle complex geometries. The numerical model completely parallelized using the MPI library and can be executed on high performance computing systems.

2.3 Free surface

The free surface detrmines the boundary between the two fluids in the numerical model. The dintinguishing characteristics of the two fluids are density and viscosity. The free surface in the numerical wave tank is captured using the level set method (Osher and Sethian, 1988) and the respective material properties are applied to the two phases. Using the level set method, the interface is represented by the zero level set of the signed distance level set function ϕ. The level set function provides the least distance of each point in the domain from the interface. The different fluids are distinguished by the sign of the level set function as shown in Eq. (4):

$$\phi(\vec{x},t)\begin{cases} > 0 & if\ \vec{x}\ is\ in\ phase\ 1 \\ = 0 & if\ \vec{x}\ is\ at\ the\ interface \\ < 0 & if\ \vec{x}\ is\ in\ phase\ 2 \end{cases} \tag{4}$$

The definition of the level set function makes it smooth across the interface and provides a sharp representation of the interface. The level set function is convected by the velocity field in the numerical wave tank. The signed distance property is lost on convection and is restored by

re-initializing the level set function after every iteration with the partial differential equation re-initialization procedure by Peng et al. (1999).

2.4 Numerical wave tank

The numerical wave tank uses the relaxation method (Larsen and Dancy, 1983) for wave generation and absorption. In this method, relaxation functions are used to moderate the computational values to the expected values from wave theory to generate and absorb waves. This requires certain zones of the wave tank to be reserved as relaxation zones for wave generation and absorption. The numerical model uses the relaxation functions proposed by Jacobsen et al. (2012) presented in Eq. (5):

$$\Gamma(x) = 1 - \frac{e^{(1-x)^{3.5}} - 1}{e - 1} \tag{5}$$

where $\Gamma(x)$ is the relaxation function and x is the coordinate along the x-axis scaled to the length of the relaxation zone. The relaxation functions prescribe the required values for free surface elevation and velocity from wave theory to the wave tank using Eq. (6):

$$\begin{aligned} u_{relaxed} &= \Gamma(x) u_{analytical} + (1 - \Gamma(x)) u_{computational} \\ \phi_{relaxed} &= \Gamma(x) \phi_{analytical} + (1 - \Gamma(x)) \phi_{computational} \end{aligned} \tag{6}$$

The relaxation function also absorbs reflections from the objects placed in the numerical wave tank, so that it does not affect wave generation and simulates a wavemaker with active absorption. At the numerical beach, the computational values from the wave tank are reduced to zero to smoothly absorb wave energy without spurious reflections from the beach. No-slip boundary condition is applied on the bottom wall an the surface of the objects in the tank and symmetry boundary conditions on the top of the numerical wave tank and is enforced through the ghost cell immersed boundary method.

3 Results

A grid refinement study is carried out first to select the grid size to be used for the simulations in the study. Then, wave propagation over a submerged bar are simulated for different incident wave heights and the numerical results are compared to experimental data. The wave transformation over the submerged bar is studied using the data obtained from the wave gages at different locations along the length of the bar. The evolution of spilling and plunging breakers on the bar crest in the simulation is also presented. The shoaling process for the different incident waves is examined through the variation of the relative wave crest elevations. The decomposition process with transfer of wave energy to higher harmonics is examined by calculating the power spectral densities of the computed free surface elevations at the different locations in the wave tank.

3.1 Grid refinement study

Accurate wave generation and propagation in the numerical wave tank is verified by carrying out a grid refinement study. A two-dimensional wave tank of length 38 m and height 0.8 m is

used to generate second-order Stokes waves with wave period $T = 2.5$ s, wavelength $L = 4.74$ m and wave height $H_1 = 0.022$ m in a water depth of $d = 0.4$ m. Grid sizes $dx = 0.04$ m, 0.02 m, 0.01 m and 0.005 m are used. The results presented in Fig. (1) show that the free surface elevations converge to the required values from a grid size of $dx = 0.02$ m onwards. Due to the high order discretization schemes used in the model and the relatively low wave steepness in the study, there is no significant difference in the wave heights obtained at the different grid sizes. But, in order to capture the evolution of wave shoaling and breaking in this study, a grid size of $dx = 0.005$ m is used for the simulations.

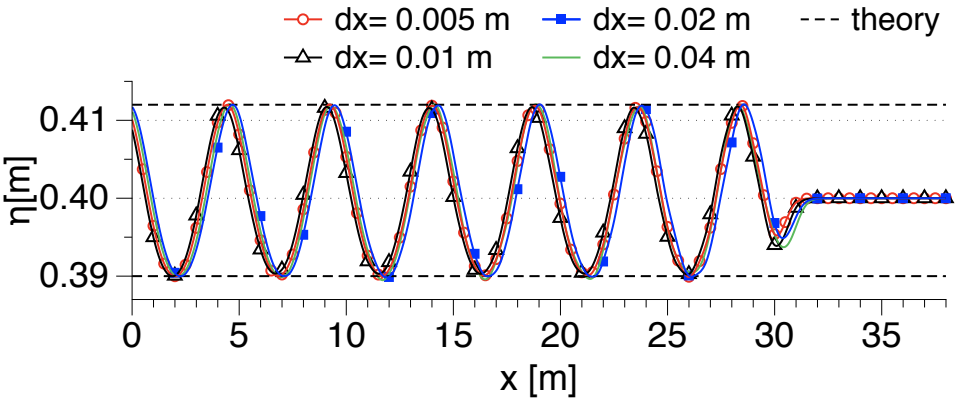

Figure 1: Grid refinement study with $2nd$-order Stokes waves of T=2.5 s and $H_1 = 0.022$ m

In addition to the grid refinement study for wave generation and propagation int he numerical wave tank without any obstacles, a grid refinement study for the plunging breaking wave obtained for $H_4 = 0.052$ m is carried out with simulations at grid sizes $dx = 0.005$ m, 0.01 m, 0.02 m and 0.04 m. This is done to verify that the grid resoltuion is sufficient for the representation of the complex case of wave breaking. From the free surface profiles in Fig. (2), it can be concluded that the breaker location has converged to $x = 17.2$ m from $dx = 0.01$ m onwards, but the vertical profile of the breaking wave crest is best represented by $dx = 0.005$ m. This confirms that the choice of $dx = 0.005$ m as the grid size for the simulations is justified. The very fine grid required to represent the wave breaking in this study arises from the fact that the incident waves are of low steepness and they undergo large and rapid changes in their wave steepness during propagation over the bar. This follows the conclusions by Alagan Chella et al. (2015), that incident waves with lower steepnesses undergo larger deformations than waves with larger incident steepnesses. The computational time required for this fine grid simulation is about 40 hours on 128 processors for a simulation length of 60 s.

3.2 Numerical wave tank setup

The simulations of wave propagation over a submerged bar are carried out based on the experimental studies by Beji and Battjes (1993). The submerged bar has a weather side slope of 1 : 20, a lee side slope of 1 : 10 and a crest height of 0.3 m. The wave tank has a water depth of $d = 0.4$ m resulting in a depth of 0.1 m on the crest of the bar and incident waves of heights $H_1 = 0.022$ m, $H_2 = 0.035$ m, $H_3 = 0.042$ m and $H_4 = 0.052$ m are simulated. Wave

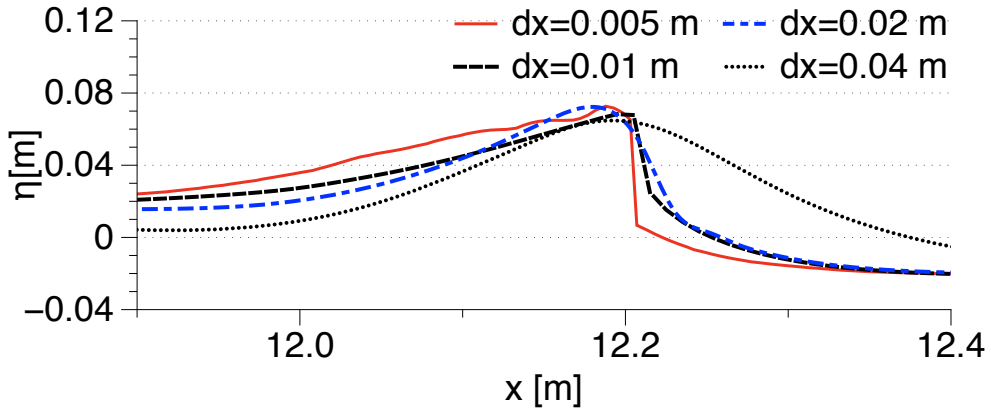

Figure 2: Grid refinement study for plunging breaker location for $H_4 = 0.052$ m

gages are placed at various locations along the bar to evaluate the wave propagation over the bar as shown in Fig. (3). A two-dimensional numerical wave tank 38 m long and 0.8 m high with a grid size of 0.005 m is used, resulting in a total of 1.216 million cells. A CFL number of 0.1 is used. A wave generation relaxation zone of length 5 m and a numerical beach of length 9.5 m are used at the beginning and the end of the wave tank respectively to ensure good wave generation and absorption. The $x-$coordinate in the wave tank begins at the end of the wave generation relaxation zone and the same distances as in the experiments by Beji and Battjes (1993) are maintained. An overview of the simulations carried out is presented in Table 1.

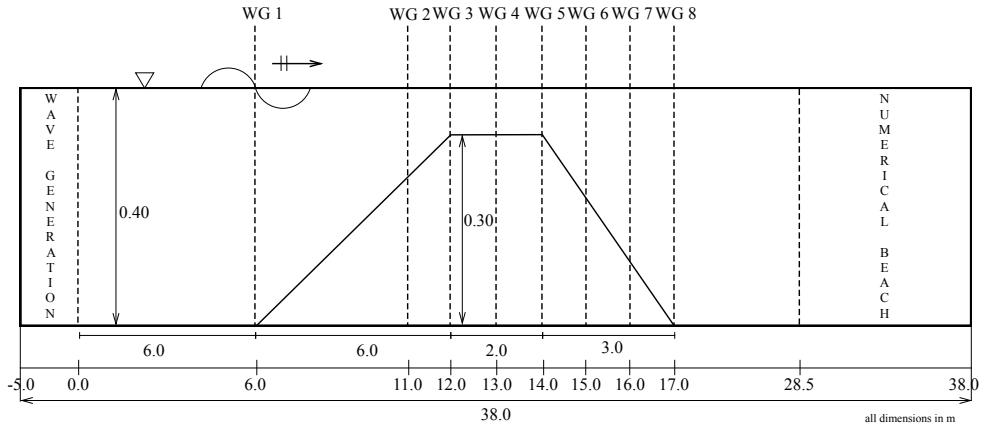

Figure 3: Schematic diagram of the setup used in the numerical simulations, all dimensions in m

3.3 Non-breaking wave propagation over a submerged bar

A simulation is carried out with second-order Stokes waves of wave height $H_1 = 0.022$ m, wave period $T = 2.5$ s and wavelength $L = 4.74$ m. The free surface elevations are computed

Table 1: Summary of the results from the different simulations in the study

Test	T (s)	H (m)	ξ	ϵ_{max}	breaking type
1.	2.5	0.022	1.4678	0.1275	non-breaking
2.	2.5	0.035	1.1637	0.2008	non-breaking
3.	2.5	0.042	1.0623	0.0526	spilling
4.	2.5	0.052	0.9547	0.0641	plunging

at several locations along the submerged bar and are compared with the measured experimental data in Fig. (4) and a good agreement is seen in both the phase and amplitude of the transformed waves. As the waves propagate along the reducing water depth along the upward slope of the bar, the wave profile is seen to be slightly deformed with the development of a saw-toothed profile at $x = 11.0$ m in Fig. (4b), which becomes prominent at $x = 12.0$ m in Fig. Fig. (4c). As a result of wave shoaling, high and sharp wave crests are formed over the bar crest $x = 13.0$ m in Fig. (4d). The decomposition of the wave with the development of higher harmonic components is also observed from $x = 14.0$ m (Fig. 4e) onwards, as the wave propagates over the end of the bar crest. As the wave propagates along the lee side slope of the bar, the water depth increases and a process opposite to wave shoaling takes place as described by Beji and Battjes (1993). The free surface elevation begins to reduce compared to the elevations on the upward slope and the crest. The wave decomposition results in the formation of secondary and tertiary waves after the bar crest as seen in Figs. 4f, 4g, 4h.

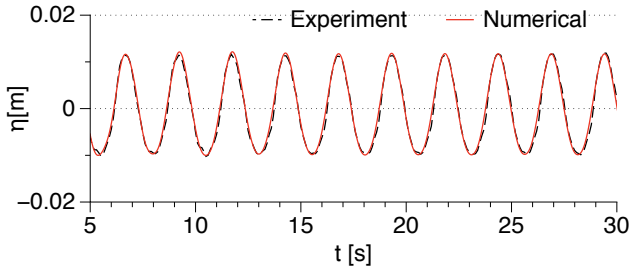

(a) WG 1, x= 6.0 m

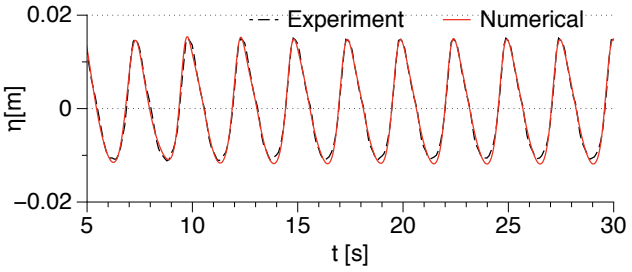

(b) WG 2, x= 11.0 m

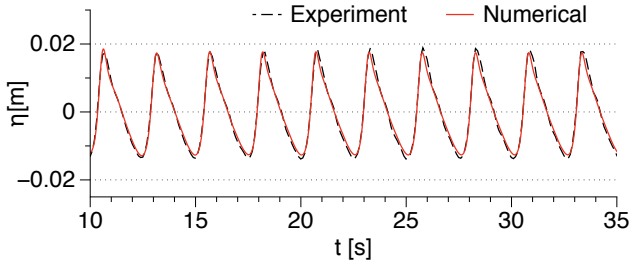

(c) WG 3, x= 12.0 m

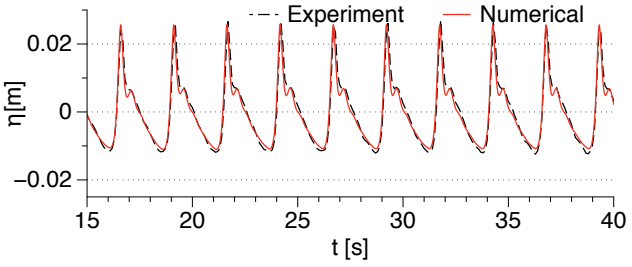

(d) WG 4, x= 13.0 m

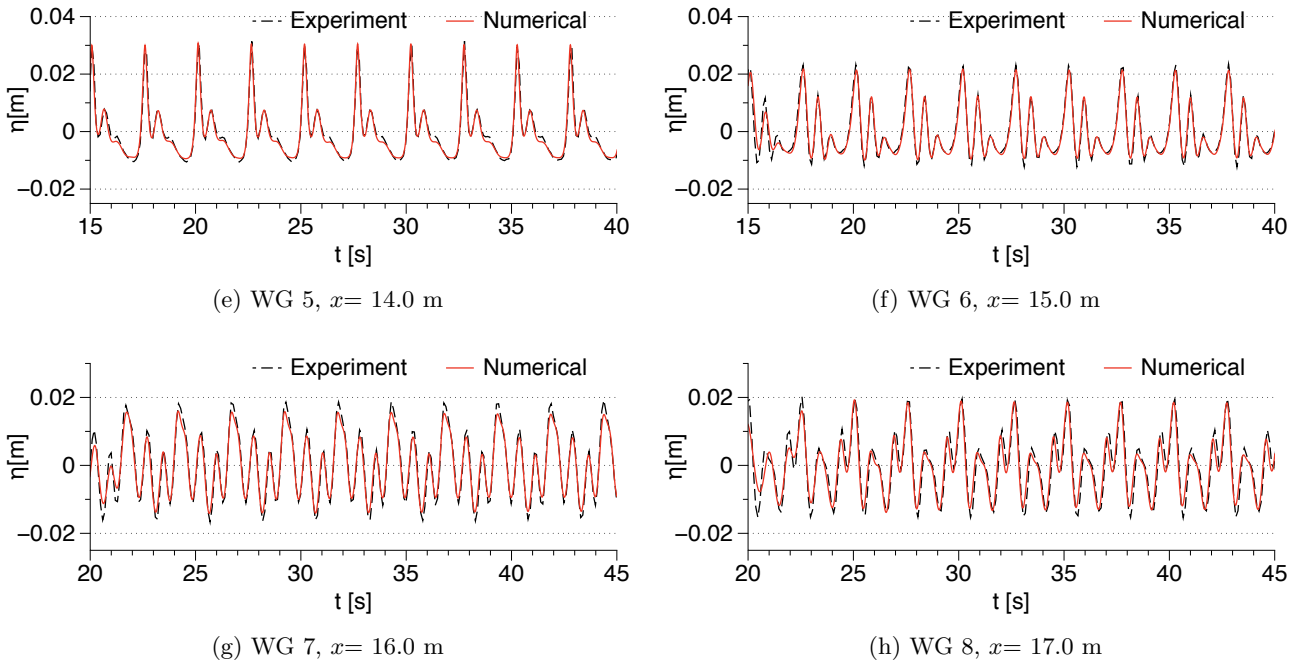

(e) WG 5, x= 14.0 m

(f) WG 6, x= 15.0 m

(g) WG 7, x= 16.0 m

(h) WG 8, x= 17.0 m

Figure 4: Free surface elevations at various locations along the wave flume for $H_1 = 0.022$ m

3.4 Breaking wave propagation over a submerged bar

The incident wave height is further increased to $H_3 = 0.042$ m to simulate spilling breakers and the computed free surface elevations are compared with experimental data in Fig. (5). The computed results show a good agreement with the experimental data at most of the locations but some differences are seen in the amplitudes computed at $x = 13.0$ m, 14.0 m and 15.0 m, though the wave phases are in good agreement. This is due to the fact that the wave breaks over the crest of the bar, between $x = 13.0$ m and $x = 14.0$ m. The average difference between the primary wave crest heights in the numerical results and the experimental data are found to be about 0.012 m over a 25 s window which is 24% of the local wave height. The complex flow scenario due to small scale wave breaking over very shallow water ($d = 0.1$ m) over the bar crest results in instantaneous changes in the pattern of the free surface elevations in this region. It is challenging to capture these free surface effects resulting from violent mixing of air and water, both experimentally and numerically in the near post-breaking region. This accounts for the difference observed in the free surface elevations at $x = 13.0$ m and $x = 14.0$ m in Fig. (5d) and (5e). The difference in the wave crest height reduces to 0.0036 m over a 25 s window at WG 7 at $x = 16.0$ m and the numerical results for WG 8 at $x = 17.0$ m match the experimental results again.

The evolution of the wave profile in the region of wave breaking in the simulation is presented in Fig. (6) to obtain further insight into the breaking process in this case. The shoaling of the wave due to the reducing water depth leads to a sharp wave crest on the bar crest as seen in Fig. (6a). The bar crest acts as a flat bottom with very low water depth and the wave propagates over the crest without much change to its amplitude, but with reduced wave celerity. The reduction in wave celerity combined with an increase in wave crest elevation due

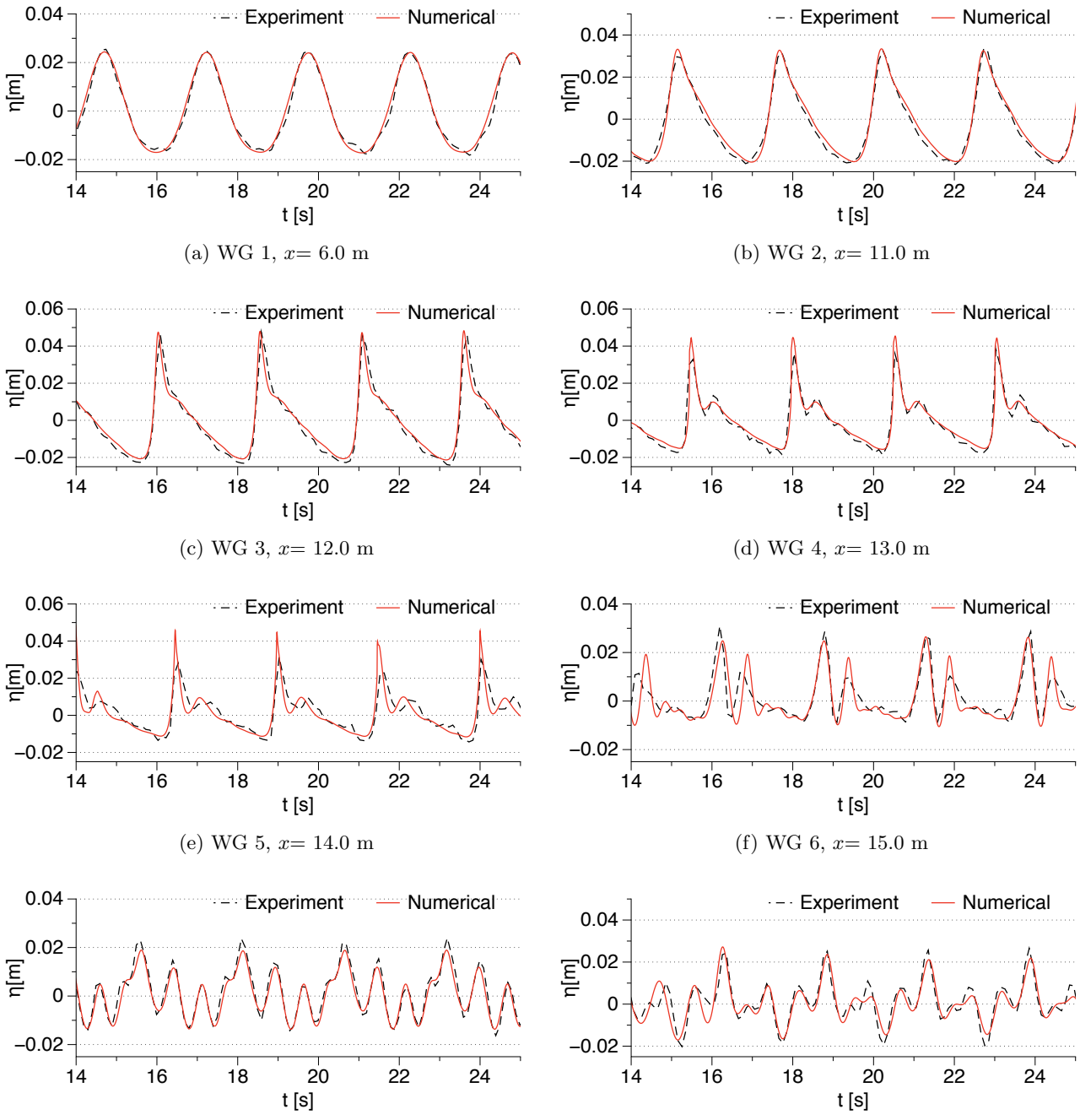

(a) WG 1, x= 6.0 m

(b) WG 2, x= 11.0 m

(c) WG 3, x= 12.0 m

(d) WG 4, x= 13.0 m

(e) WG 5, x= 14.0 m

(f) WG 6, x= 15.0 m

(g) WG 7, x= 16.0 m

(h) WG 8, x= 17.0 m

Figure 5: Free surface elevations at various locations along the wave flume for $H_3 = 0.042$ m

to shoaling leads to a local imbalance in the wave energy with wave crest particle velocities higher than the wave celerity. This increases the asymmetry of the wave and the appearance of a steep wave crest. The steep wave crest then stretches away from the main wave crest in Fig. (6b). Due to lack of further excess energy, the wave crest then begins to spill forward

onto the main wave crest in Figs. (6c) and (6d), resulting in a small scale spilling breaker. The velocity contours in the figures demonstrate the large increase in the horizontal water particle velocity in the overturning crest compared to the rest of the free surface, signifying the complex hydrodynamics involved in the spilling breaking wave. The total duration from the near vertical wave crest profile until the wave crest rejoins the preceding trough is only $0.1T$, signifying the rapid and small scale nature of the spilling breaker in this case. Similarly the evolution of the plunging breaking wave over the bar crest for H4 = 0.052 m is shown in Figures 7(a)-7(e).

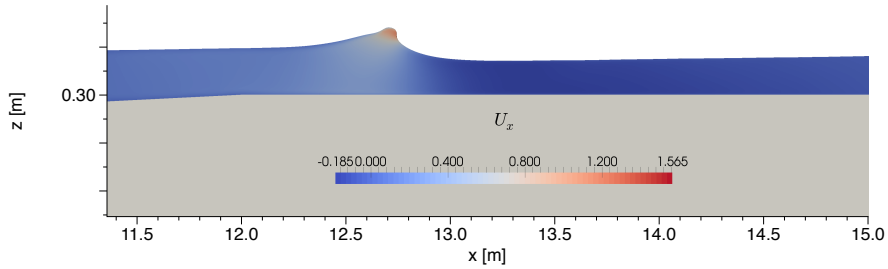

(a) t/T=8.89

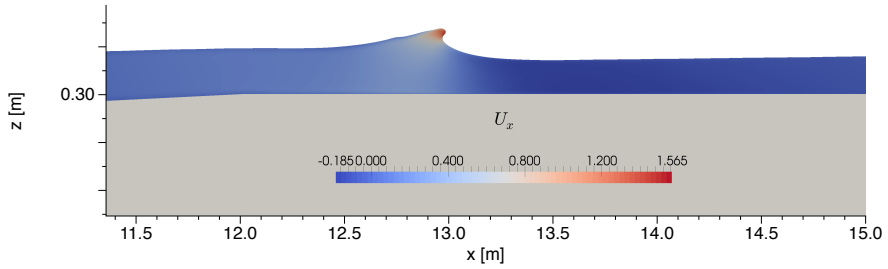

(b) t/T=8.93

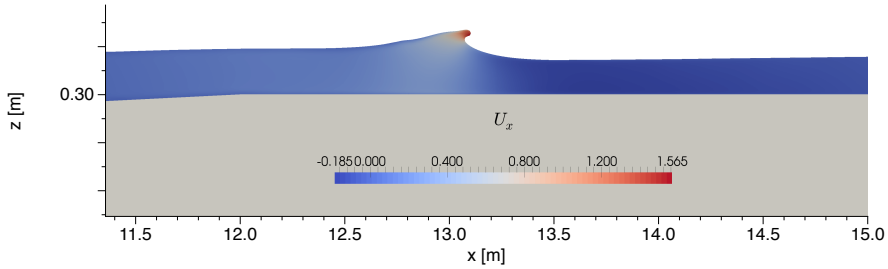

(c) t/T=8.95

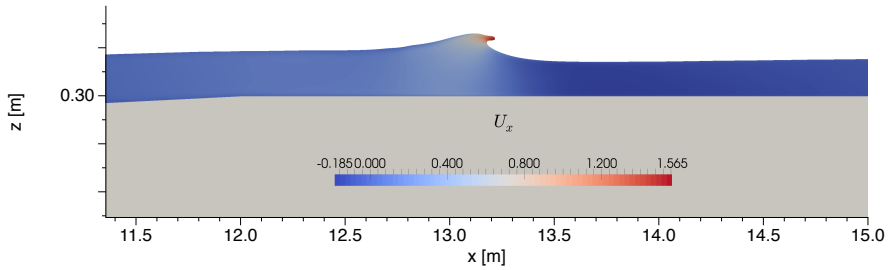

(d) t/T=8.97

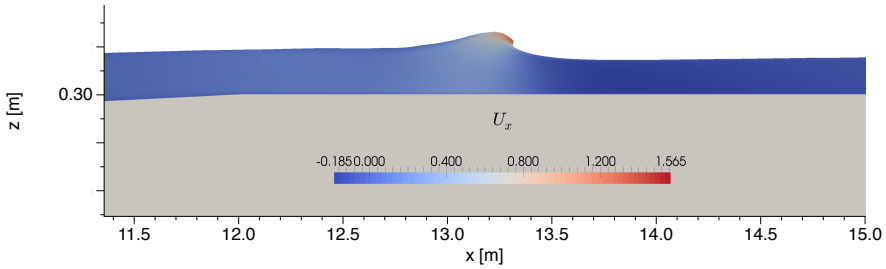

(e) t/T=8.99

Figure 6: Process of spilling wave breaking over the bar crest for $H_3 = 0.042$ m

3.5 Wave transformation process

The variation in the relative wave crest elevations computed at the different wave gages is studied to gain a comparative perspective of the wave transformation process for both non-breaking and breaking waves. The incident waves at $x = 6.0$ m in Fig. (8a) show the small horizontal asymmetry in the wave profile with shallower troughs and sharper crests, which is characteristic of second-order Stokes waves. The breaking and non-breaking waves show certain differences in the transformation properties. In the case of the non-breaking waves with $H_1 = 0.022$ m and $H_2 = 0.035$ m, shoaling leads to saw-toothed asymmetry in the wave profile. The higher incident wave H_2 undergoes a higher increase in the relative crest elevation and attains a sharper saw-toothed asymmetry in Fig. (8b) at $x = 11.0$ m. As the wave reaches the crest of the bar at $x = 12.0$ m, the relative crest elevation is higher for H_2 compared to H_1 in Fig. (8c). In the region over the bar crest at $x = 13.0$ m and $x = 14.0$ m, the higher incident wave maintains a higher relative crest elevation in Figs. (8d) and (8e). The maximum wave crest steepness (Kjeldsen and Myrhaug, 1978) $\epsilon = \eta'/L'$, where η' is the wave crest height and L' the distance from the wave crest to the wave zero-crossing location, can be used to quantify the crest steepness. In the case of $H_2 = 0.035$ m, the maximum wave crest steepness $\epsilon_{max} = 0.2008$ is calculated for WG 4 at $x = 13.0$ m. The maximum wave crest steepness $\epsilon_{max} = 0.1275$ for $H_1 = 0.022$ m is obtained at $x = 14.0$ m at WG 5. Also, the higher incident wave (H_2) moves faster than the lower incident wave (H_1). This follows from shallow water wave propagation, where a higher wave propagates faster for a given wave period and water depth. The higher incident wave attains the highest crest elevation during its propagation over the upward slope and thus propagates faster over the shallow water depth over the crest. The submerged bar crest ends at $x = 14.0$ m and the initiation of wave decomposition is seen in Fig. (8e), with the appearance of secondary crests. As the wave propagates further, the water depth increases over the downward slope of the submerged bar. This change in the water depth begins a process of de-shoaling (Beji and Battjes, 1993), where the waves reduce in amplitude as they propagate over gradually increasing water depths. Well-developed secondary wave crests are seen at $x = 15.0$ m in Fig. (8f). It is also observed that the reduction in the relative crest elevation is lower for the lower incident wave. The higher non-breaking wave H_2, which had the highest crest elevation at $x = 13.0$ m has a lower primary crest elevation and a higher secondary crest elevation compared to H_1, indicating that H_2 transfers a larger amount of wave energy to a higher frequency. In Figs. (8g) and (8h), the formation of a secondary and a tertiary wave crest is seen for both the non-breaking waves. The lower

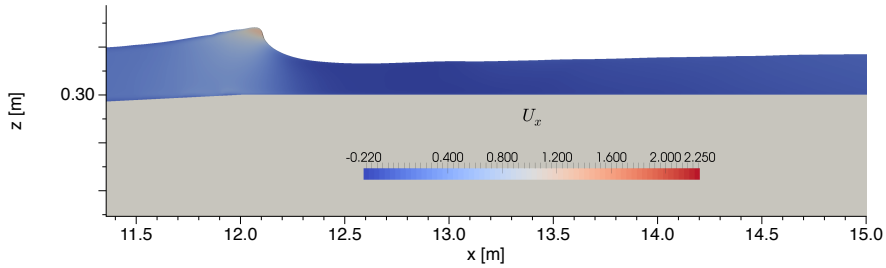

(a) t/T=7.74

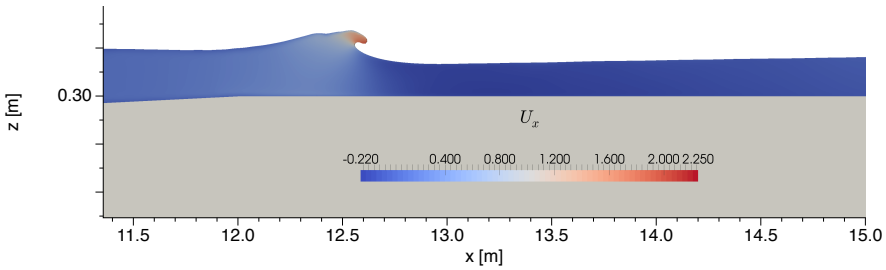

(b) t/T=7.82

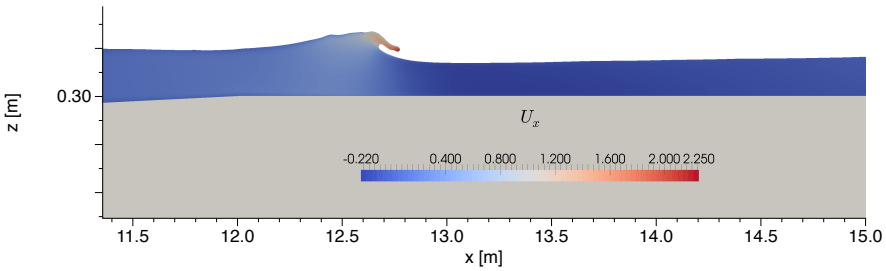

(c) t/T=7.84

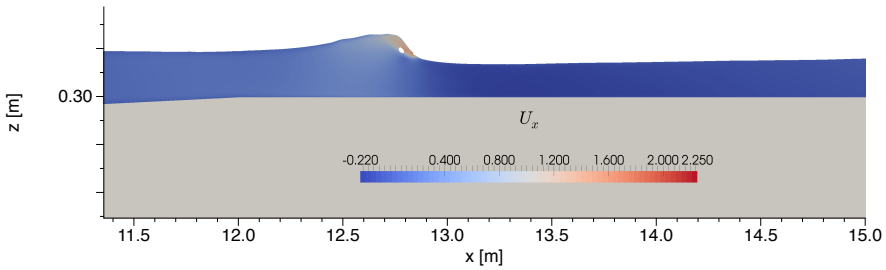

(d) t/T=7.86

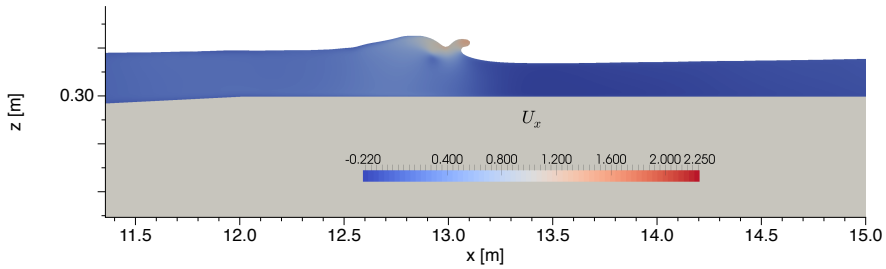

(e) t/T=7.90

Figure 7: Process of plunging wave breaking over the bar crest for $H_4 = 0.052$ m

wave (H_1) continues to maintain a higher primary relative crest elevation throughout the wave decomposition process, whereas the higher wave has slightly higher secondary and tertiary relative crest elevations.

In the case of $H_3 = 0.042$ m and $H_4 = 0.052$ m spilling and plunging wave breaking is observed between $x = 12.0$ m and $x = 13.0$ m. During the shoaling process from $x = 6.0$ m to $x = 12.0$ m shown in Figs. (8b) and (8c), the waves have similar relative elevations. The breaking waves attain their maximum wave crest steepness of $\epsilon_{max} = 0.0526$ for H_3 and $\epsilon_{max} = 0.0641$ for H_4 at WG 3 at $x = 12.0$ m. At the wave gages after the breaking region, $x = 13.0$ m to $x = 17.0$ m, H_3 maintains a higher relative crest elevation in Figs. (8d)-(8h).

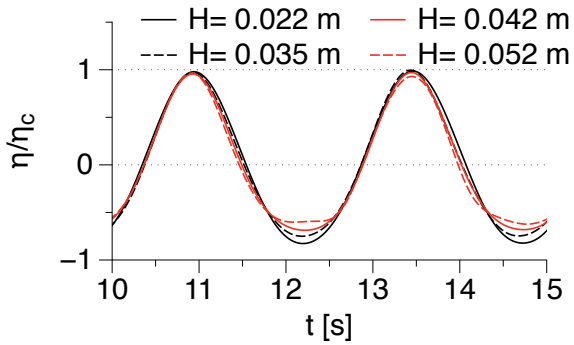

(a) WG 1, x= 6.0 m

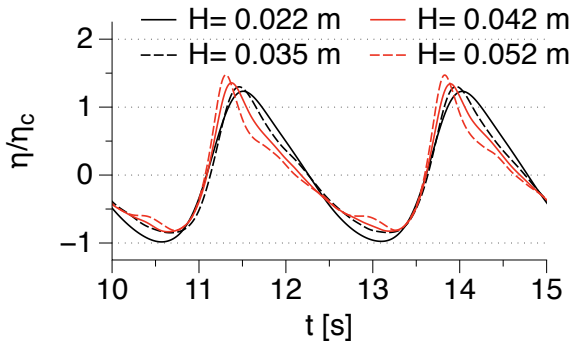

(b) WG 2, x= 11.0 m

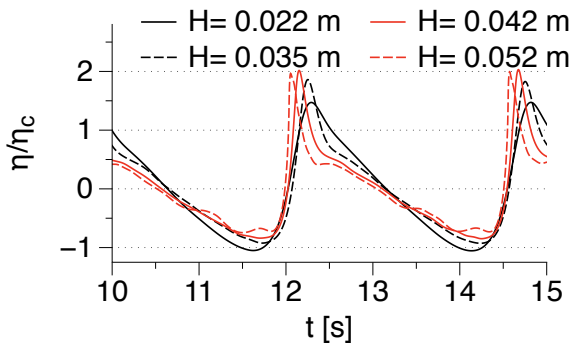

(c) WG 3, x= 12.0 m

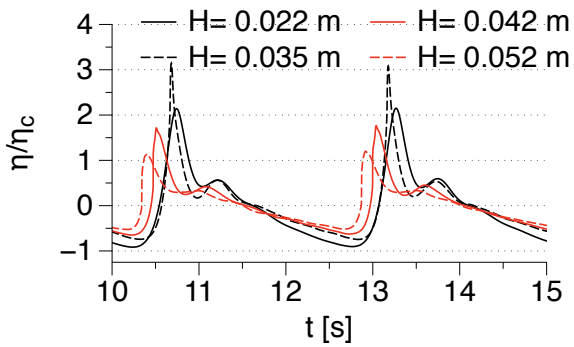

(d) WG 4, x= 13.0 m

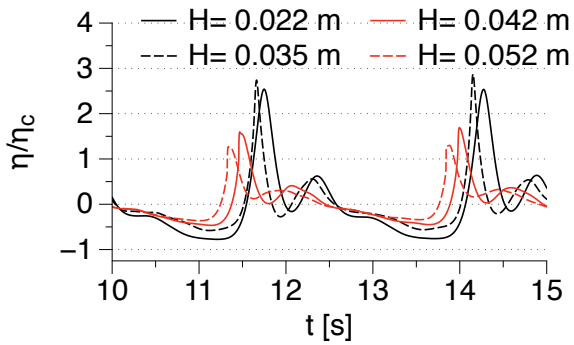

(e) WG 5, x= 14.0 m

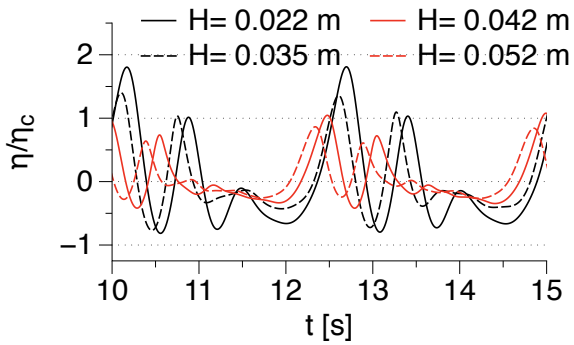

(f) WG 6, x= 15.0 m

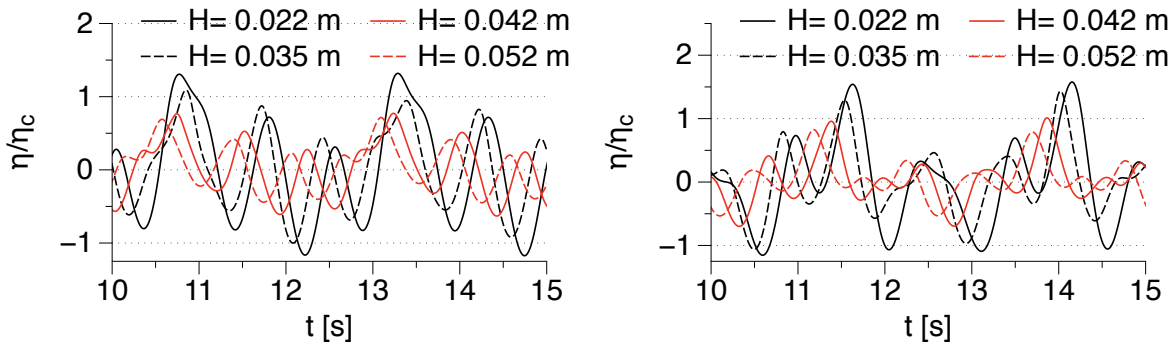

(g) WG 7, x= 16.0 m

(h) WG 8, x= 17.0 m

Figure 8: Relative free surface elevations at various locations along the wave flume for the different wave heights simulated

This is justified by the fact that H_4 evolves into a plunging breaking wave and dissipates a larger part of its energy in the process compared to the spilling breaking wave formed by H_3. It is also noticed that the surf similarity number is $\xi = 1.0623$ for H_3 and $\xi = 0.9547$ for H_4. According to the classification by Battjes (1974), these correspond to plunging wave breaking on an emergent plane slope, but the results in this study show a spilling breaker for H_3 and plunging breaker for H_4. This indicates that the wave breaking on a bar crest has different breaker characteristics and the original classification for wave breaking on emergent plane slopes can not be directly applied to wave breaking over a submerged bar.

In order to further understand the wave transformation process for the different cases simulated, the phase difference between the different waves during their propagation over the bar is analysed at the various gage locations. The relative phase difference $\delta\theta$ is calculated as:

$$\delta\theta = \frac{360^\circ \delta x}{L} \tag{7}$$

where δx is the horizontal distance between the two primary wave crests and L is the wavelength.

The relative phase difference $\delta\theta$ between the primary wave crests for $H_2 = 0.035$ m, $H_3 = 0.042$ and $H_4 = 0.052$ m with respect to $H_1 = 0.022$ m is presented in Fig. (9). It can be concluded that the higher waves propagate faster and keep gaining on the lower incident waves until the bar crest ends. The phase differences between the free surface elevations show that H_4 leads H_1 by a maximum $\delta\theta_{14} = 60^\circ$ at $x = 14.0$ m. Over the lee side of the bar, the primary wave crests undergo a sudden reduction in their celerity during the decomposition process with H_2 lagging H_1 by $\delta\theta_{12} = 11.46^\circ$ and H_4 leading H_1 by only $\delta\theta_{14} = 27.94^\circ$ at $x = 16.0$ m (WG 7). As the waves propagate further to $x = 17.0$ m (WG 8), the phase differences return to the values obtained at the end of the bar crest at $x = 14.0$ m (WG 5). Thus, the wave transformation process for all the incident waves is similar up to the region of wave breaking, with a higher incident wave attaining a higher relative crest elevation. After the region of wave breaking, the transformation of the breaking waves depends on the type of wave breaking, whereas the non-breaking waves continue with the trend seen on the weather side slope. In the region of increasing water depth after the bar crest, the lower non-breaking

wave maintains a higher primary relative crest elevation compared to the secondary relative crest elevation. The breaking waves show similar relative crest amplitudes. The higher incident waves are also seen to propagate faster and increase in celerity over the bar up to the end of the bar crest.

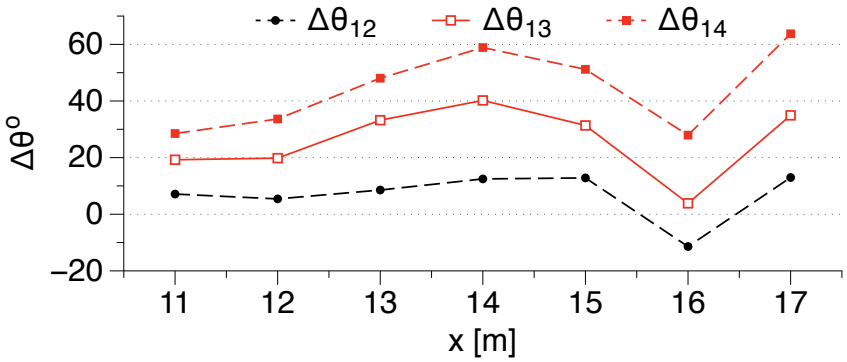

Figure 9: Relative phase difference between primary wave crests in the different cases simulated in the study with respect to the lowest incident wave with $H_1 = 0.022$ m

3.6 Wave decomposition process

The wave decomposition process is examined by calculating the power spectral densities from the free surface elevations at the different locations for the different cases presented in the study. The location of the peaks in the spectra are used to identify the harmonics to which the wave energy is transferred during wave decomposition. The free surface elevations are provided to the Fast Fourier Transform (FFT) algorithm with a sampling interval of t_s =0.01 s over a simulation period of 60 s resulting in 6000 FFT points. Zero-padding is applied to obtain total input points to the closest power of 2, that is, 8192 points. The Nyquist frequency is 50 Hz. The normalized power spectra at the different wave gage locations along the bar are presented in Fig. (10). The power spectra for all the cases are normalized with the spectral amplitude at the primary wave frequency, $f_0 = 0.4$ Hz, S_{max} in Fig. (10a). The process of shoaling results in an increase of the energy content at the primary frequency and the first harmonic of the non-breaking waves. The lowest incident wave, H_1, adds $0.25S_{max}$ to its fundamental frequency f_0 whereas H_2 and H_3 gain 0.12 and 0.16 S_{max} respectively at the first harmonic at $x = 11.0$ m. On the other hand, the spectral power density for the highest incident wave H_4 is reduce by $0.05S_{max}$ at f_0 and increased by $0.14S_{max}$ at the first harmonic f_1. At $x = 12.0$ m, the waves reach the bar crest, and significant spectral densities are obtained up to the fourth harmonic f_4 with $0.024S_{max}$ for H_4. Wave breaking occurs between $x = 12.0$ m and $x = 13.0$ m for H_3 and H_4. This corresponds with a reduction of the spectral power density to $0.368S_{max}$ for H_3 and $0.272S_{max}$ for H_4 at f_0 at $x = 13.0$ m. In the case of the non-breaking waves, H_1 retains $0.82S_{max}$ at f_0 and transfers $0.20S_{max}$ and $0.11S_{max}$ to f_1 and f_2 respectively. As the waves propagate across the bar crest and in the region of increasing water depth at $x = 15.0$ m, the major portion of the energy is distributed between f_0 and f_2 for H_1. For H_2, H_3 and H_4 the major portion of the energy is distributed amongst f_0, f_2 and f_3 at $x = 15.0$ m in Fig. (10f). At $x = 16.0$ m, the spectral power density

for all the four waves is mainly concentrated at f_0 and f_2 in Fig. (10g). As the waves reach a water depth of $d = 0.4$ m again at $x = 17.0$ m, H_1 has similar power densities of $0.24S_{max}$ and $0.20S_{max}$ at f_0 and f_1 respectively and $0.31S_{max}$ at f_2.

The variation of the spectral power density in the first four harmonics over the submerged bar for all the four waves is presented in Fig. (11). The power spectral density at f_0 is reduced significantly at $x = 17.0$ m to $0.24S_{max}$, $0.11S_{max}$, $0.09S_{max}$ and $0.09S_{max}$ for H_1, H_2, H_3 and

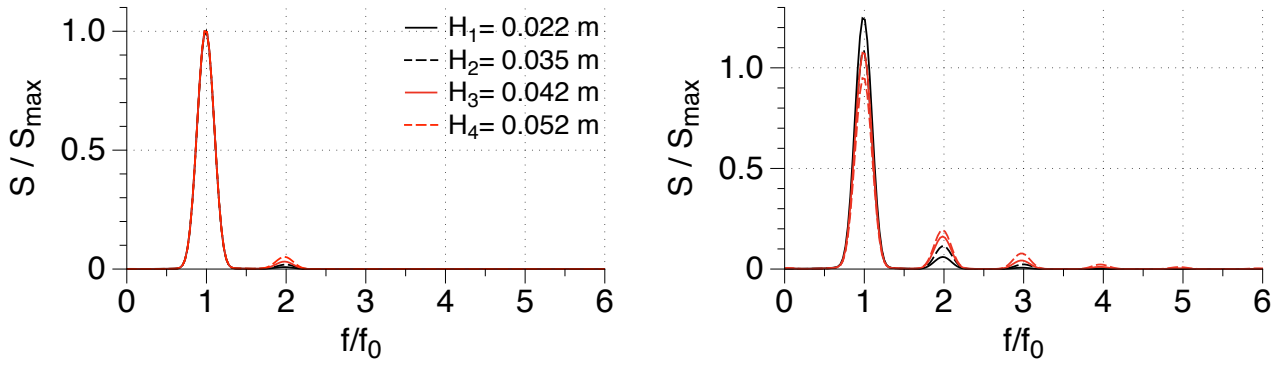

(a) WG 1, $x = 6.0$ m

(b) WG 2, $x = 11.0$ m

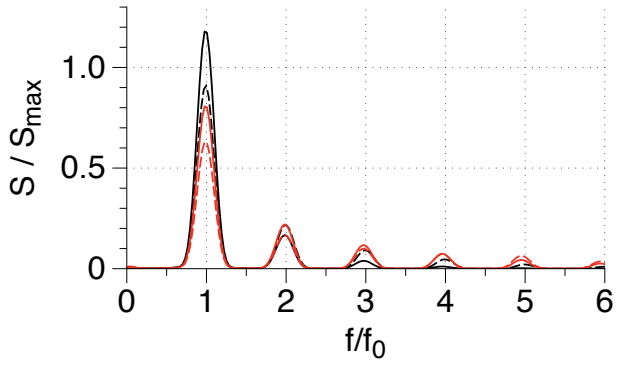

(c) WG 3, $x = 12.0$ m

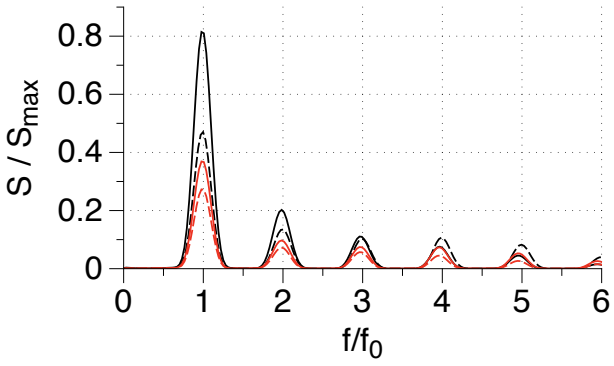

(d) WG 4, $x = 13.0$ m

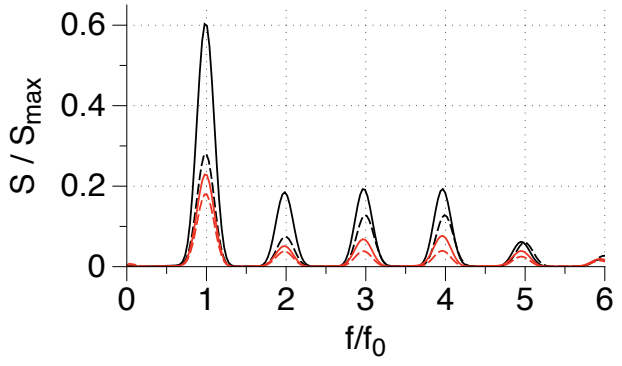

(e) WG 5, $x = 14.0$ m

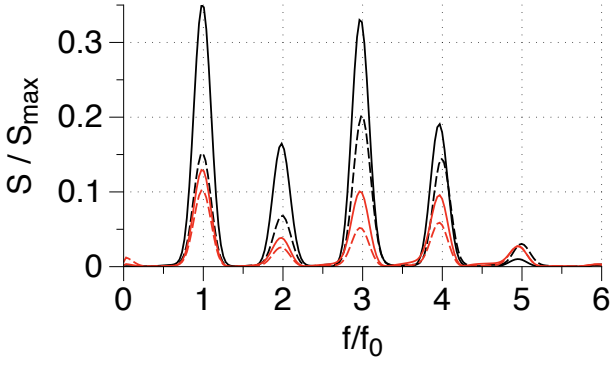

(f) WG 6, $x = 15.0$ m

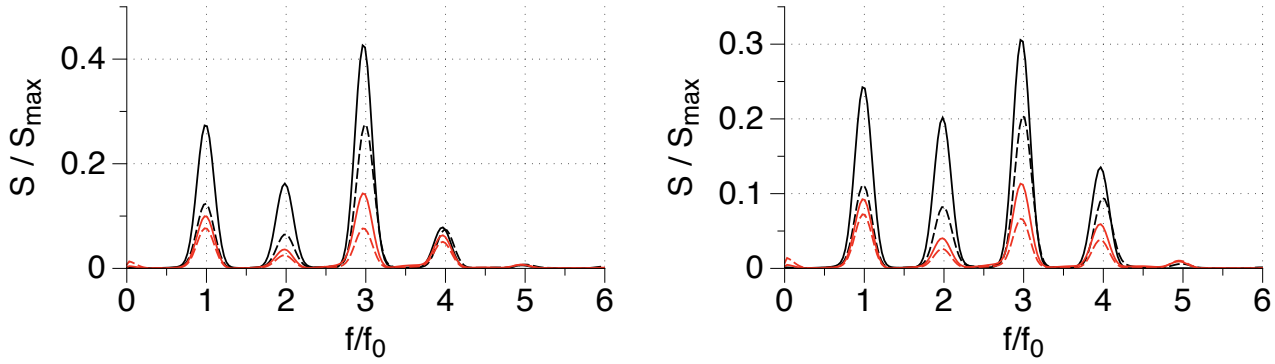

(g) WG 7, $x = 16.0$ m (h) WG 8, $x = 17.0$ m

Figure 10: Normalized spectra for the simulated waves showing decomposition of the incident wave into higher harmonics

H_4 respectively in Fig. (11a). From Fig. (11b), it is seen that the first harmonic f_1 initially gains energy in all the cases, but loses this energy gradually in all the cases except H_1.

The second harmonic f_2 gradually gains energy as the waves propagate over the bar, with a maximum of $0.42S_{max}$ at $x = 16.0$ m for H_1 in Fig. (11c). The maximum spectral power in the third harmonic f_3 appears between $x = 14.0$ m and $x = 15.0$ m in Fig. (11d). The following

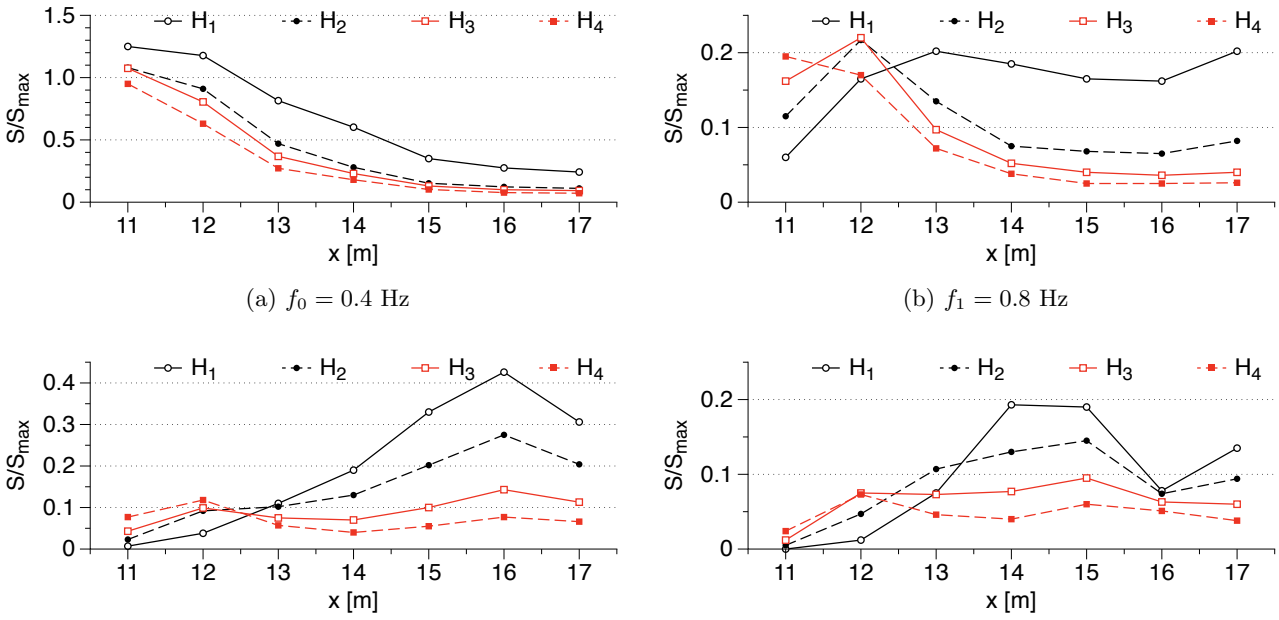

(a) $f_0 = 0.4$ Hz (b) $f_1 = 0.8$ Hz

(c) $f_2 = 1.2$ Hz (d) $f_3 = 1.6$ Hz

Figure 11: Variation of the normalized power density spectra at the first four harmonics for the different incident waves along the submerged bar

distinct pattern emerges regarding the energy transfer between the different harmonics. The fundamental frequency gradually loses most of its energy as the wave propagates over the bar. The first harmonic gains energy initially on the weather side slope, but loses this energy gradually. The second harmonic gains energy steadily and holds most of the wave energy towards the end of the bar. The third harmonic contains significant amounts of energy in the intermediate stages between $x = 13.0$ m and $x = 15.0$ m. Finally, the variation of the total energy in the first four harmonics over the length of the bar for all the cases is presented in Fig. (12). It is clear that all the waves lose significant amounts of energy except for H_1, with total spectral power densities of $0.89S_{max}$, $0.49S_{max}$, $0.31S_{max}$ and $0.30S_{max}$ for H_1, H_2, H_3 and H_4 respectively at $x = 17.0$ m, losing $1.25S_{max}$, $0.53S_{max}$, $0.73S_{max}$ and $0.85S_{max}$ during propagation over the bar.

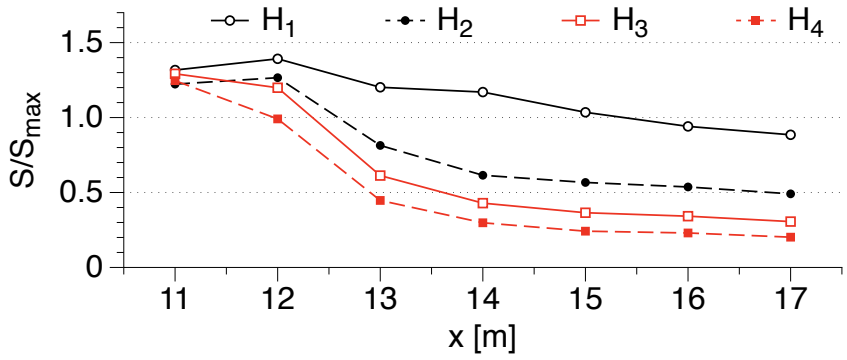

Figure 12: Variation of the total normalized power spectral density for the different incident waves along the submerged bar

4 Effect of lee side slope on wave decomposition

After a thorough investigation of the wave transformation and decomposition process over a submerged bar, the effect of the lee side slope on the wave decomposition process is studied for non-breaking wave with $H_2 = 0.035$ m, spilling breaking wave with $H_3 = 0.042$ m and plunging breaking wave with $H_4 = 0.052$ m. Additional simulations are carried out using leeside slopes of $1 : 5$ and $1 : 20$ and compared to the results obtained for the lee side slope of $1 : 10$ in the previous section. The free surface elevations are measured at relative distances $x_r = x_g - x_t/L$, where x_g is the gage location, x_t is the location of the leeside toe and L is the wavelength. The free surface elevations at $x_r = -0.10$, 0.0, 0.21 and 0.84 are measured and the spectral power density is calculated.

The normalised power density spectra at various locations over the submerged bar for $H_2 = 0.035$ m are presented in Fig.(13). It is seen that most of the wave energy is present in the second harmonic $f/f_0 = 3$ for all the three lee side slopes. The wave energy in the fundamental frequency $f/f_0 = 1$ is similar for all the three slopes over the region after the submerged bar. In the case of the steeper lee side slope of $m = 1 : 5$, significant energy is contained in the third harmonic $f/f_0 = 4$ at $x_r = -0.10$ and this energy is dissipated as the wave propagates to $x_r = 0.84$. On the other hand, for the milder slope of $m = 1 : 20$, the

wave energy is mostly concentrated in the second harmonic $f/f_0 = 3$ and is reduced by 50% as the wave propagates from $x_r = -0.10$ to 0.84. The waves propagating over the mildest slope with $m = 1:20$ generally have the lowest energy in the three slopes studied. Thus, for non-breaking waves, a steeper slope leads to energy transfer to the second and third harmonics and a a milder slope results in higher energy in the second harmonic.

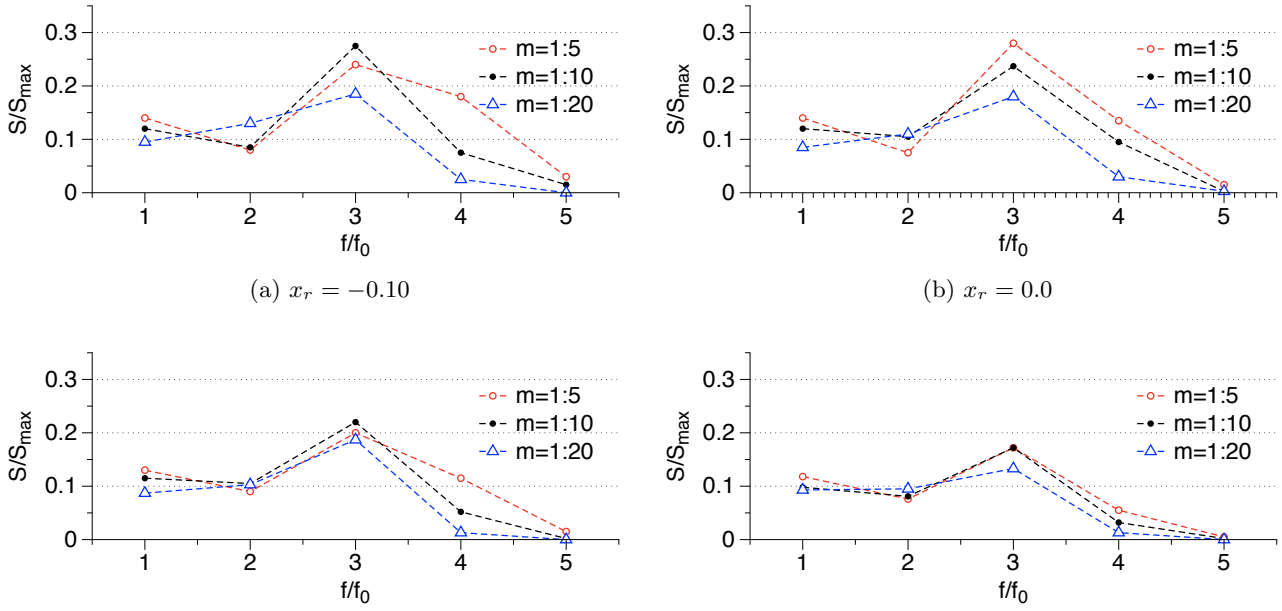

(a) $x_r = -0.10$ (b) $x_r = 0.0$

(c) $x_r = 0.21$ (d) $x_r = 0.84$

Figure 13: Variation of the normalized power density spectra at different locations along the submerged bar for the non-breaking wave with H_2 =0.035 m

In the case of the spilling breaking waves with incident wave height $H_3 = 0.042$ m, the normalised power spectral density is calculated using the free surface elevations at $x_r = -0.10$, 0.0, 0.21 and 0.84 and the results are presented in Fig.(14). Due to the wave breaking process, the wave energy at $x_r = -0.10$ is lower in this case in Fig.(14a) compared to the non-breaking waves, but the pattern of the wave energy distribution amongst the harmonics is similar. The wave energy for both slopes $m = 1:5$ and $1:20$ is lower than that for $m = 1:10$ at $x_r = -0-10$. Over the lee side toe of the bar at $x_r = 0.0$, the energy distribution for $m = 1:5$ and $m = 1:10$ are similar up to the second harmonic, whereas the steeper slope allows for more energy in the third harmonic. In the case of the milder slope $m = 1:20$, the wave energy is the lowest amongst the three over all the harmonics except the first harmonic. On propagating further, the wave energy in the fundamental frequency is retained at similar values for all the three slopes, whereas the wave energy in the higher harmonics is reduced significantly, in Figs.(14c and 14d). Thus, for spilling breaking waves, the lee side slope does not have a strong influence on the wave transformation and decomposition process after wave breaking. The maximum energy is contained in the second harmonic for all the three slopes studied.

The normalised spectral power density at different locations over a submerged bar for

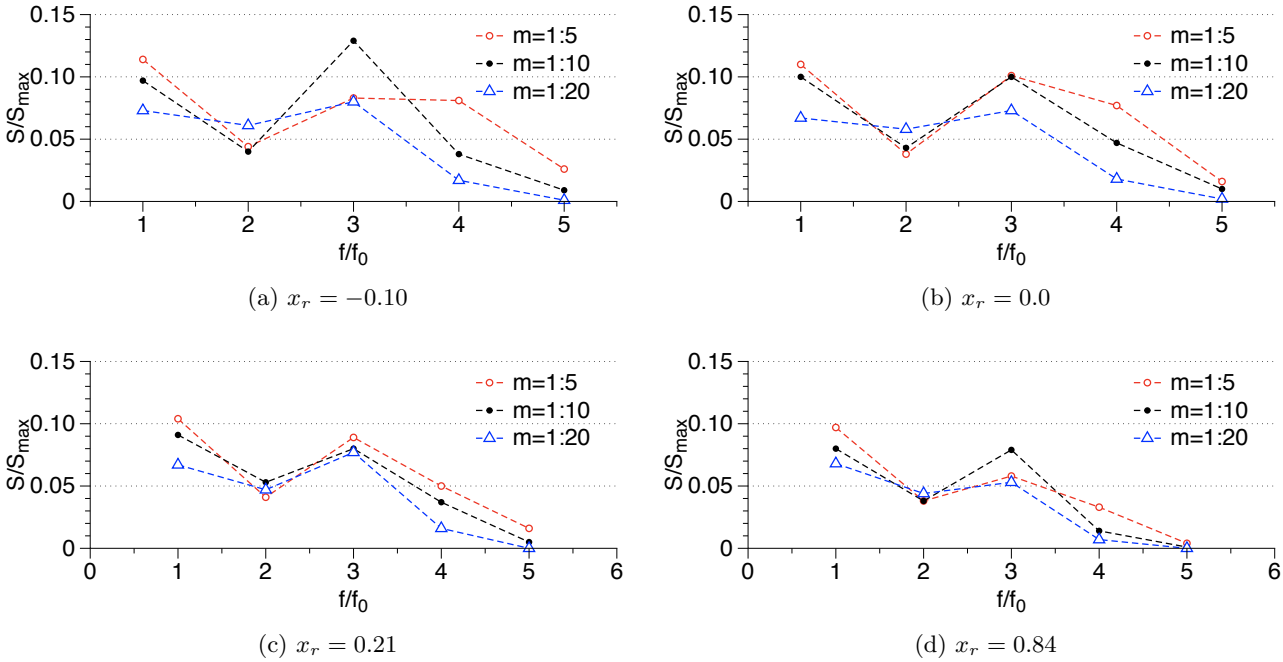

(a) $x_r = -0.10$ (b) $x_r = 0.0$

(c) $x_r = 0.21$ (d) $x_r = 0.84$

Figure 14: Variation of the normalized power density spectra at different locations along the submerged bar for the spilling breaking wave with H_3 =0.042 m

plunging breaking waves propagating over different lee side slopes is presented in Fig.(15). Similar to the spilling breaking waves, the lee side slope of $m = 1 : 10$ has the highest energy in the third harmonic $f/f_0 = 3$. The waves propagating over the steepest slope of $m = 1 : 5$ have the highest energy in the fundamental frequency $f/f_0 = 1$. Thus, a steeper lee side slope results in higher wave energy being retained in the fundamental and second harmonic while a milder slope results in lower energy in the fundamental frequency. The main difference between the case with spilling breaking and plunging breaking is the higher total energy loss in the case of plunging braking waves.

From the results for the wave decomposition process for non-breaking, spilling breaking and plunging breaking waves propagating over different lee side slopes, it is seen that a steeper slope results in the retention of larger amounts of energy in the fundamental frequency. On

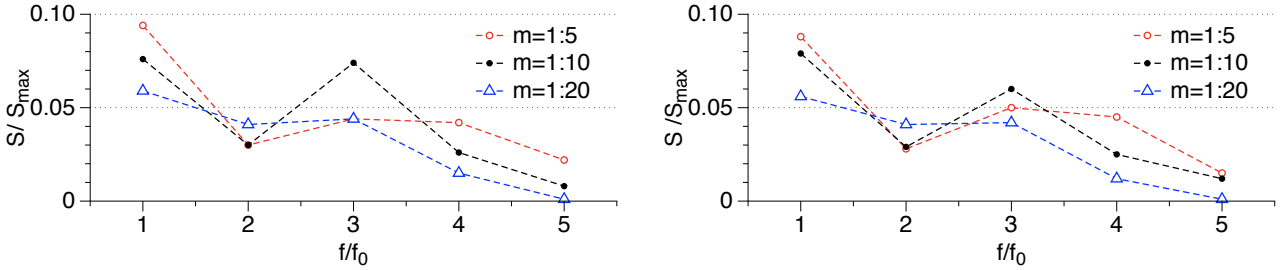

(a) $x_r = -0.10$ (b) $x_r = 0.0$

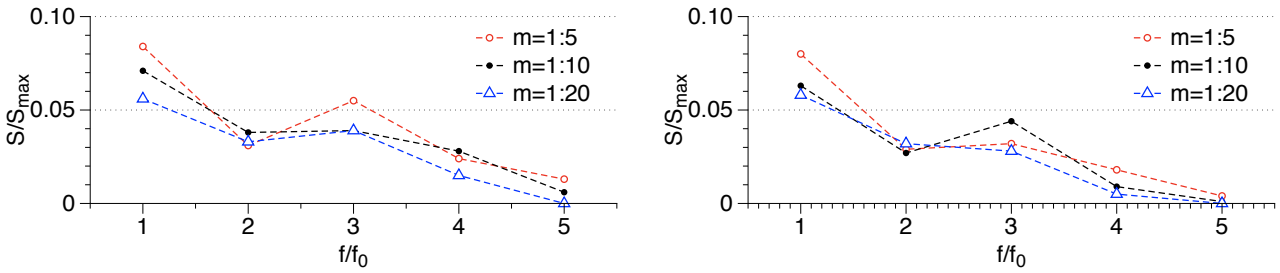

(c) $x_r = 0.21$ (d) $x_r = 0.84$

Figure 15: Variation of the normalized power density spectra at different locations along the submerged bar for the plunging breaking wave with H_3 =0.052 m

the other hand a milder lee side slope results in lower energy in the fundamental frequency and also lower total energy in the propagating wave. In the context of combining a submerged bar with a floating breakwater, these results indicate that the submerged bar constructed in front of the floating breakwater should have sufficiently mild slope in order to decompose the incident to shorter waves for efficient absorption by the floating breakwater.

5 Conclusion

The open-source CFD model, REEF3D is used to simulate wave propagation over a submerged bar including wave shoaling, breaking and decomposition for regular long waves with $T = 2.5$ s. The computed free surface elevations at several locations along the length of the flume are compared with experimental data and a general good agreement is seen both in terms of the phase and the elevation of the free surface variation for both non-breaking and spilling breaking waves. A good representation of the wave shoaling and decomposition of the wave on the weather side and lee side slopes respectively is obtained in the simulations. The high order discretization schemes in the model result in realistic modeling of the non-linear wave interactions and the dispersion characteristics of the decomposing waves for the more challenging case with long waves with $T = 2.5$ s, showing strong decomposition on the lee side of the bar. Spilling breakers are observed on the bar crest for an incident wave height of 0.042 m (ξ =1.0623) and on further increase of the incident wave height to 0.052 m (ξ = 0.9547), plunging breakers are observed. A difference of about 24% of the local wave height is seen in the near post-breaking region due to the complex air-water interaction. The wave transformation and decomposition is thoroughly analyzed and the following conclusions are made regarding the wave transformation process along the bar:

- Non-breaking waves with higher incident amplitude increase in crest elevation until the end of the bar crest.
- Breaking waves with higher incident amplitude increase in crest elevation until the breaking region on the bar crest.
- Breaker classification using the surf similarity numbers based on emergent sloping beaches can not be applied directly in this scenario.

- Higher incident waves keep increasing their celerity and gain in wave phase over the lower wave heights until end of the bar crest.

The power spectra of the free surface elevations along the bar provided the following results regarding the wave decomposition process:

- Significant reduction in the wave energy at the fundamental frequency is seen for all the cases simulated and higher incident waves transfer a larger amount of energy to their higher harmonics on the weather side slope.
- A distinct pattern is observed in energy transfer amongst the harmonics with the first, second and third harmonics containing their maximum energies at the initial, the final and in the intermediate stages over the bar respectively.
- A steeper lee side slope results in larger energy retention in the fundamental frequency, whereas a milder lee side slope effectively decomposes the incident wave to its second harmonic.

The current study presents an analysis of regular wave propagation over a submerged bar for non-breaking and breaking waves along with the energy and free surface transformations involved. The study can be extended to irregular wave propagation over a submerged bar along with the effect of the weather side and lee side slope of the bar and the length of the bar crest on the wave transformation and decomposition. Further, the interaction of the waves with a combined submerged bar and floating breakwater to provide effective coastal protection with minimum visual impact on the coastline can be investigated.

References

Adeyemo, M.D. (1968). Effect of beach slope and shoaling on wave asymmetry. In: *Proceedings of the 11th Conference on Coastal Engineering*, volume 1, 145–172.

Alagan Chella, M., Bihs, H., Myrhaug, D. and Muskulus, M. (2015). Breaking characteristics and geometric properties of spilling breakers over slopes. *Coastal Engineering*, **95**, 4–19.

Battjes, J.A. (1974). Surf similarity. In: *Proc., 14th International Conference on Coastal Engineering, Copenhagen, Denmark*, 466–480.

Beji, S. and Battjes, J.A. (1993). Experimental investigation of wave propagation over a bar. *Coastal Engineering*, **19**, 151–162.

Beji, S. and Battjes, J.A. (1994). Numerical simulation of nonlinear wave propagation over a bar. *Coastal Engineering*, **23**, 1–16.

Berthelsen, P.A. and Faltinsen, O.M. (2008). A local directional ghost cell approach for incompressible viscous flow problems with irregular boundaries. *Journal of Computational Physics*, **227**, 4354–4397.

Bihs, H., Kamath, A., Alagan Chella, M., Aggarwal, A. and Arntsen, Ø.A. (2016). A new level set numerical wave tank with improved density interpolation for complex wave hydrodynamics. *Computers & Fluids*, **140**, 191–208.

Blenkinsopp, C.E. and Chaplin, J.R. (2008). The effect of crest submergence on wave breaking over submerged slopes. *Coastal Engineering*, **55**, 967–974.

Bosboom, J., Klopman, G., Roelvink, J. and Battjes, J. (1996). Wave kinematics computations using boussinesq models. In: *Proc. 25th International Conference on Coastal Engineering, Orlando, USA*, 109–122.

Bradshaw, P., Ferriss, D.H. and Atwell, N.P. (1967). Calculation of boundary layer development using the turbulent energy equation. *Journal of Fluid Mechanics*, **28**, 593–616.

Brocchini, M. (2013). A reasoned overview on boussinesq-type models: the interplay between physics, mathematics and numerics. In: *Proceedings of the Royal Society*, volume 469, 20130496.

Brocchini, M., Drago, M. and Iovenitti, L. (1992). The modelling of short waves in shallow water. comparison of numerical methods based on boussinesq and serre equations. In: *Proc. 23rd International Conference on Coastal Engineering, New York, USA*.

Chang, K.A., Hsu, T.J. and Liu, P.L.F. (2001). Vortex generation and evolution of water waves propagating over a submerged rectangular obstacle. part i. solitary waves. *Coastal Engineering*, **44**, 13–36.

Chau, K.W. and Jiang, Y.W. (2001). 3d numerical model for pearl river estuary. *Journal of Hydraulic Engineering*, **127**(1), 72–82.

Chau, K.W. and Jiang, Y.W. (2004). A three-dimensional pollutant transport model in orthogonal curvilinear and sigma coordinate system for Pearl river estuary. *International Journal of Environment and Pollution*, **21**(2), 188–198.

Choi, H. and Moin, P. (1994). Effects of the computational time step on numerical solutions of turbulent flow. *Journal of Computational Physics*, **113**, 1–4.

Chorin, A. (1968). Numerical solution of the Navier-Stokes equations. *Mathematics of Computation*, **22**, 745–762.

Christensen, E.D. (1998). Turbulence in breaking waves – a numerical investigation. PhD thesis.

Christensen, E.D. (2006). Large eddy simulation of spilling and plunging breakers. *Coastal Engineering*, **53**(5–6), 463–485.

Christensen, E.D. and Deigaard, R. (2001). Large eddy simulation of breaking waves. *Coastal Engineering*, **42**, 53–86.

Durbin, P.A. (2009). Limiters and wall treatments in applied turbulence modeling. *Fluid Dynamics Research*, **41**, 1–18.

Gourlay, M.R. (1994). Wave transformation on a coral reef. *Coastal Engineering*, **23**, 17–42.

Haun, S., Olsen, N.R.B. and Feurich, R. (2011). Numerical modeling of flow over trapezoidal broad-crested weir. *Engineering Applications of Computational Fluid Mechanics*, **5**(3), 397–405.

Hieu, P.D., Katsutoshi, T. and Ca, V.T. (2004). Numerical simulation of breaking waves using a two-phase flow model. *Applied Mathematical Modeling*, **28**(11), 983–1005.

Jacobsen, N.G., Fuhrman, D.R. and Fredsøe, J. (2012). A wave generation toolbox for the open-source CFD library: OpenFOAM. *International Journal for Numerical Methods in Fluids*, **70**(9), 1073–1088.

Jiang, G.S. and Peng, D. (2000). Weighted ENO schemes for Hamilton-Jacobi equations. *SIAM Journal on Scientific Computing*, **21**, 2126–2143.

Jiang, G.S. and Shu, C.W. (1996). Efficient implementation of weighted ENO schemes. *Journal of Computational Physics*, **126**, 202–228.

Kamath, A., Alagan Chella, M., Bihs, H. and Arntsen, Ø.A. (2015). Cfd simulations of wave propagation and shoaling over a submerged bar. *Aquatic Procedia*, **4**, 308–316.

Kjeldsen, S. and Myrhaug, D. (1978). *Kinematics and dynamics of breaking waves*. River and Harbour Laboratory (NHL) The Norwegian Institute of Technology.

Kobayashi, N., Otta, A. and Roy, I. (1987). Wave reflection and runup on rough slopes. *Journal of Waterway, Port, Coastal and Ocean Engineering*, **3**(113), 282–298.

Lai, W. and Khan, A.A. (2012). Discontinuous galerkin method for 1D shallow water flows in natural rivers. *Engineering Applications of Computational Fluid Mechanics*, **6**(1), 74–86.

Larsen, J. and Dancy, H. (1983). Open boundaries in short wave simulations - a new approach. *Coastal Engineering*, **7**, 285–297.

Lemos, C.M. (1992). A simple numerical technique for turbulent flows with free surfaces. *International Journal of Numerical Methods in Fluids*, **15**, 127–146.

Lin, P. and Liu, P.L.F. (1998). A numerical study of breaking waves in the surf zone. *Journal of Fluid Mechanics*, **359**, 239–264.

Lubin, P., Vincent, S., Abadie, S. and Caltagirone, J.P. (2006). Three-dimensional large eddy simulation of air entrainment under plunging breaking waves. *Coastal engineering*, **53**(8), 631–655.

Mo, W., Jensen, A. and Liu, P.L.F. (2013). Plunging solitary wave and its interaction with a slender cylinder on a sloping beach. *Ocean Engineering*, **74**, 48–60.

Morgan, G.C.J., Zang, J., Greaves, D., Heath, A., Whtilow, C.D. and Young, J.R. (2010). Using the rasinterfoam CFD model for wave transformation and coastal modeling. In: *Proc., Coastal Engineering Conference, Shanghai, China*, 1–9.

Muttil, N. and Chau, K.W. (2007). Machine-learning paradigms for selecting ecologically significant input variables. *Engineering Applications of Artificial Intelligence*, **20**(6), 735–744.

Naot, D. and Rodi, W. (1982). Calculation of secondary currents in channel flow. *Journal of the Hydraulic Division, ASCE*, **108**(8), 948–968.

Osher, S. and Sethian, J.A. (1988). Fronts propagating with curvature- dependent speed: algorithms based on Hamilton-Jacobi formulations. *Journal of Computational Physics*, **79**, 12–49.

Peng, D., Merriman, B., Osher, S., Zhao, H. and Kang, M. (1999). A PDE-based fast local level set method. *Journal of Computational Physics*, **155**, 410–438.

Roeber, V., Cheung, K. and Kobayashi, M. (2010). Shock-capturing boussinesqtype model for nearshore wave processes. *Coastal Engineering*, **57**, 407–423.

Stelling, G. and Zijlema, M. (2003). An accurate and effcient fnite-difference algorithm for non-hydrostatic free-surface fow with application to wave propagation. *International Journal for Numerical Methods in Fluids*, **43**, 1–23.

Tissier, M., Bonneton, P., Marche, F., Chazel, F. and Lannes, D. (2012). A new approach to handle wave breaking in fully non-linear boussinesq models. *Coastal Engineering*, **67**, 54–66.

van der Vorst, H. (1992). BiCGStab: A fast and smoothly converging variant of Bi-CG for the solution of nonsymmetric linear systems. *SIAM Journal on Scientific and Statistical Computing*, **13**, 631–644.

Watanabe, Y., Saeki, H. and Hosking, R.J. (2005). Three-dimensional vortex structures under breaking waves. *Journal of Fluid Mechanics*, **545**, 291–328.

Wilcox, D.C. (1994). *Turbulence modeling for CFD.* DCW Industries Inc., La Canada, California.

Wu, C.L. and Chau, K.W. (2006). Mathematical model of water quality rehabilitation with rainwater utilisation: a case study at Haigang. *International Journal of Environment and Pollution*, **28**(3-4), 534–545.

Zhao, Q., Armfield, S. and Tanimoto, K. (2004). Numerical simulation of breaking waves by a multi-scale turbulence model. *Coastal Engineering*, **51**(1), 53–80.